Supplementary Information: Origin of enhanced muon-spin relaxation rate in superconducting Sr_2RuO_4

Yongwei Li[1*], Rustem Khasanov[2], Paul Chekhonin[3], Julien Garaud[4], Stephen P. Cottrell[5], Zurab Guguchia[2], Hubertus Luetkens[2], Hans-Henning Klauss[6], Binru Zhao[7], Jie Ma[7], Naoki Kikugawa[8], Yoshiteru Maeno[9,10], Vadim Grinenko[1*]

[1*]State Key Laboratory of Micro-nano Engineering Science, Tsung-Dao Lee Institute & School of Physics and Astronomy, Shanghai Jiao Tong University, Shanghai, 201210, China.
[2]PSI Center for Neutron and Muon Sciences CNM, 5232 Villigen PSI, Switzerland.
[3]Helmholtz-Zentrum Dresden-Rossendorf, D-01328 Dresden, Germany.
[4]Institut Denis Poisson CNRS/UMR 7013, Universite de Tours, 37200, France.
[5]STFC-ISIS Facility, Rutherford Appleton Laboratory, Harwell Campus, Chilton, Oxfordshire, OX11 0QX, United Kingdom.
[6]Institute for Solid State and Materials Physics, Technische Universität Dresden, 01062 Dresden, Germany.
[7]School of Physics and Astronomy, Shanghai Jiao Tong University, Shanghai, 201210, China.
[8]National Institute for Materials Science, Tsukuba, 305-0003, Japan.
[9]Toyota Riken - Kyoto-Univ. Research Center (TRiKUC), Kyoto, 606-8501, Japan.
[10]Kyoto University of Advanced Science (KUAS), Kyoto, 615-8577, Japan.

*Corresponding author(s). E-mail(s): y.w.li@sjtu.edu.cn; vadim.grinenko@sjtu.edu.cn;

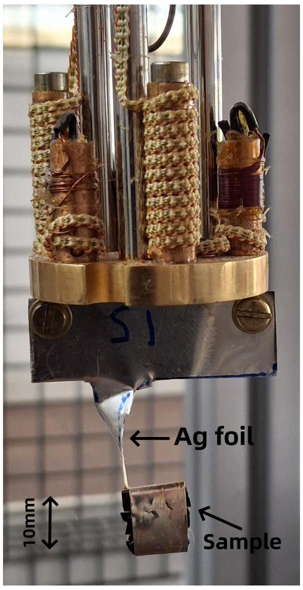

Fig. S1 Photographs of the sample mounting in the flypast configuration. The single crystals are fixed with GE varnish onto a high-purity Ag blade. A thin Ag foil is wrapped around the assembly to act as a thermal shield and to minimize the background contribution from the sample support. The muon beam with $P_\mu \parallel c$ was directed perpendicular to the sample plane.

1 Sample Mounting Details

To minimize the background signal from the sample environment, we used a flypast sample-mounting geometry. The $Sr_{2-y}La_yRuO_4$ single crystals were mounted on a high-purity silver (Ag) blade machined to match the sample dimensions (10×10 mm^2), thereby minimizing the exposed area of the holder (Fig. S1). The crystals were fixed using GE varnish to ensure both mechanical stability and good thermal contact.

A thin high-purity Ag foil was attached to the back of the blade and wrapped over the front of the crystals to serve as a radiation shield, ensuring proper thermalization of the sample at millikelvin temperatures. In this flypast configuration, muons that miss the sample do not stop in the immediate sample holder but instead continue through the cryostat toward the rear vacuum tube, effectively removing them from the relevant detection time window. The residual background signal is therefore dominated by muons scattered into the downstream cryostat walls (brass/copper), which remain at a constant temperature of approximately 1.6 K.

2 Background Analysis Details

To characterize the background contribution, we performed free fits of the ZF-μSR spectra for both of the La-doped samples ($y = 0.01$ and $y = 0.04$) using Eq. (1) without fixing the background parameters. Figure S2 summarizes the temperature dependence of the Kubo-Toyabe amplitude (A_{KT}) and the static field-distribution width ($\Delta(\mu s^{-1})$).

As shown in Fig. S2, both A_{KT} and $\Delta(\mu s^{-1})$ are essentially temperature independent over the full measured range (0.05 K to 3 K). Moreover, the values are consistent between the two samples. The static width $\Delta(\mu s^{-1})$ remains close to 0.29 μs^{-1}, and the background amplitude A_{KT} is small and stable. These results support the conclusion that the background originates from a static source at fixed temperature, namely the brass walls of the cryostat, rather than from the sample holder or the samples themselves.

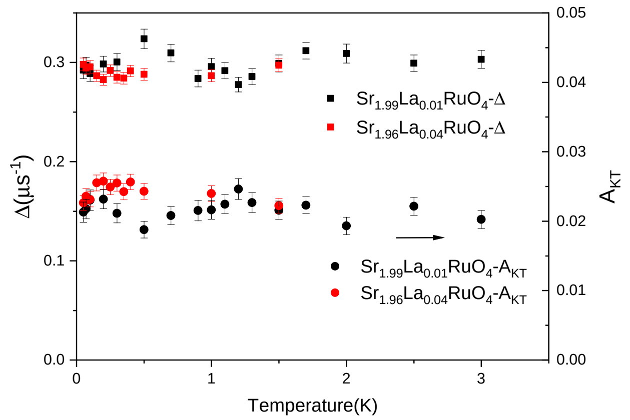

Fig. S2 Temperature dependence of the background parameters obtained from free fits of the ZF-μSR spectra for $Sr_{1.99}La_{0.01}RuO_4$ (black) and $Sr_{1.96}La_{0.04}RuO_4$ (red). The Kubo–Toyabe static width $\Delta(\mu s^{-1})$ (squares, left axis) and the background asymmetry A_{KT} (circles, right axis) show no systematic temperature dependence within the experimental uncertainty and are consistent between the two samples, confirming the static nature of the background signal.

3 Transverse Field μSR Data

Here, we present the TF-μSR data, which are primarily used to verify bulk superconductivity. Figure S3 shows the temperature dependence of the Gaussian decay rate σ for the two La-doped samples. For the $y = 0.01$ sample [Fig. S3(b)], σ increases sharply below $T_{\mathrm{c}} = 1.13(2)$ K, consistent with the formation of a bulk flux-line lattice. By contrast, for the $y = 0.04$ sample [Fig. S3(d)], σ remains constant down to the lowest measured temperature, consistent with the zero-field data and indicating that both bulk superconductivity and the BTRS-related magnetic response are fully suppressed at this doping level.

4 Specific Heat of $Sr_{2-y}La_yRuO_4$

In the main text, we argue that La substitution suppresses superconductivity relatively homogeneously rather than by generating local phase and amplitude gradients.

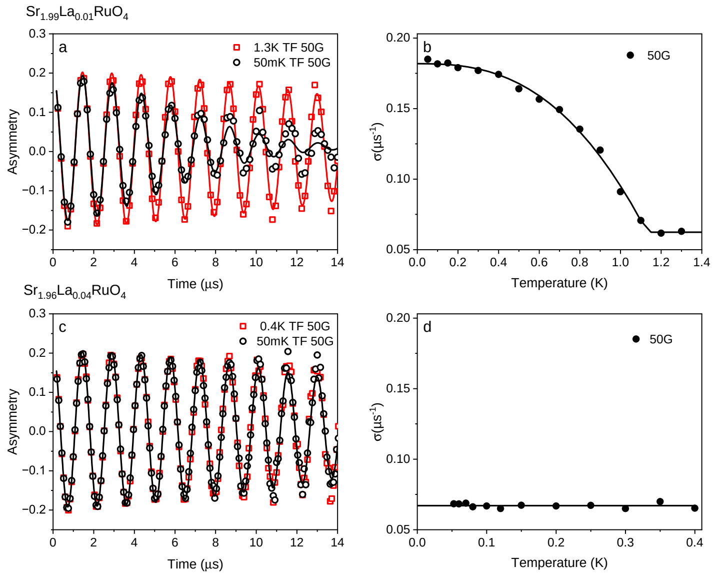

Fig. S3 TF-μSR data for $Sr_{2-y}La_yRuO_4$. (a) Time evolution of the muon-spin asymmetry for $y = 0.01$ under TF = 50 G. (b) Gaussian decay rate σ versus temperature for $y = 0.01$, showing an increase below $T_c = 1.13(2)$ K. (c) Time evolution of the muon-spin asymmetry for $y = 0.04$ under TF = 50 G. (d) σ versus temperature for $y = 0.04$. The rate remains constant, demonstrating the suppression of bulk superconductivity.

To support this view, we present the specific-heat data in Fig. S4. For each composition, the specific-heat measurement was performed on a small piece cut from the same large single crystal used in the μSR experiment. These measurements therefore provide an independent thermodynamic check of the bulk superconducting transition temperature and of the homogeneity of the crystals used for the μSR measurements. The superconducting anomaly is suppressed monotonically toward lower temperatures as the La concentration increases, without marked broadening, consistent with a relatively homogeneous distribution of La atoms.

5 T_c Correction under Magnetic Field

To compare $\Delta\Lambda$ with the zero-field superconducting transition temperature in Fig. 3, the values of T_c obtained from TF-μSR measurements must be corrected to their zero-field values (T_{c0}). To investigate the behavior of the upper critical field H_{c2} under hydrostatic pressure, we performed TF measurements at several applied magnetic fields. The resulting data are shown in Fig. S5(a). The quantity $H_{c2} \parallel c$ versus T_c for our pressure-tuned samples and for literature data on Sr_2RuO_4 follows the Werthamer-Helfand-Hohenberg (WHH) form with negligible Pauli paramagnetic effects:

$$\ln\left(\frac{T_c}{T_{c0}}\right) = \psi\left(\frac{1}{2} + \frac{C \cdot (H_{c2}/T_{c0}^2)}{T_c/T_{c0}}\right) - \psi\left(\frac{1}{2}\right), \quad (1)$$

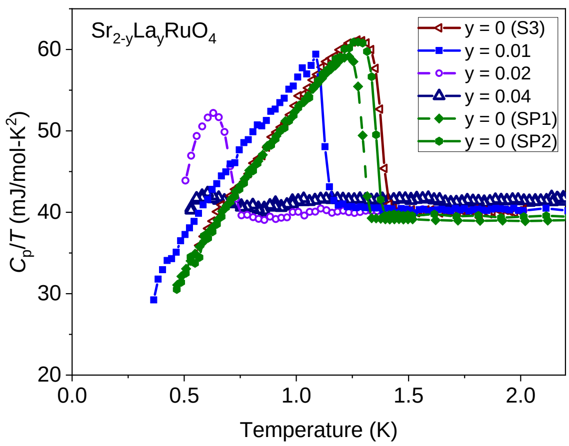

Fig. S4 Temperature dependence of the specific heat, plotted as C_p/T, for $Sr_{2-y}La_yRuO_4$ single crystals. Superconductivity is suppressed approximately homogeneously with La doping.

where $\psi(x)$ is the digamma function and $C \approx 4.06 \times 10^{-4}$ is the fitting parameter derived from the universal curve Fig. S5(b). This relation provides a practical procedure for estimating the zero-field value T_{c0} from a transition temperature measured in a single applied TF field. The normalized upper critical field H_{c2}/T_{c0}^2 versus the normalized temperature T_c/T_{c0} are shown in Fig. S5(b).

6 Absence of correlation of the spontaneous field strength with Magnetic Impurities

To test the hypothesis that the spontaneous magnetic fields, reflected in $\Delta\Lambda$, originate from dilute magnetic impurities, we performed dc magnetic susceptibility measurements on the Sr_2RuO_4 sample C171, sample C140, La-doped crystals ($y = 0.01, 0.02, 0.04$), and sample S3. The susceptibility was measured at $B = 1$ T for both zero-field-cooled (ZFC) and field-cooled (FC) protocols with $H \parallel ab$. No pronounced difference between the ZFC and FC curves was observed. Figure S6(a) shows the temperature dependence of the magnetic susceptibility $\chi(T)$. The data above 150 K were fitted using a modified Curie-Weiss form,

$$\chi(T) = \chi_0(T) + \frac{C}{T-\theta} = (a + bT) + \frac{C}{T-\theta}, \tag{2}$$

where $\chi_0(T) = a+bT$ represents the temperature-dependent nonmagnetic background, C is the Curie constant proportional to the concentration of magnetic impurities, and θ is the Weiss temperature.

Figure S6(b) plots the inverse Curie-Weiss contribution, defined as $1/(\chi-\chi_0)$. The linear temperature dependence confirms the validity of the fit in the high-temperature regime and allows us to estimate the magnetic impurity concentration in each sample through the Curie constant C.

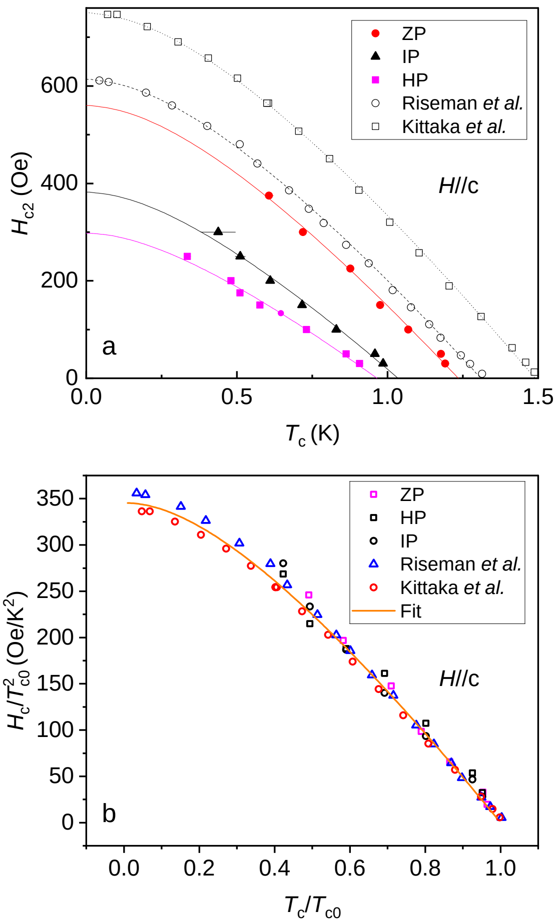

Fig. S5 (a) Superconducting upper critical field H_{c2} versus T for Sr_2RuO_4 samples from the TF-μSR measurements performed in this study (ZP: zero pressure, IP: intermediate pressure, HP: highest pressure reached in the experiment) together with literature data. (b) Normalized H_{c2}/T_{c0}^2 versus normalized critical temperature T_c/T_{c0}. The data collapse onto a universal curve described by the orbital-limited WHH model, Eq. (1).

In Fig. S6(c), we compare $\Delta\Lambda(T = 0)$ with C. If the spontaneous fields were caused primarily by magnetic impurities, one would expect $\Delta\Lambda \propto C$. No such correlation is observed. For example, the C171 sample exhibits a substantial $\Delta\Lambda$ despite a relatively small C, whereas the La-doped samples show varying C values without a corresponding monotonic trend in $\Delta\Lambda$.

To further test the relation of $\Delta\Lambda$ to magnetic impurities, we plotted $\Delta\Lambda(T = 0)$ against the maximum low-temperature value of the magnetic susceptibility, $\chi_{\max}$, in Fig. S6(d). The maximum is associated with antiferromagnetic ordering of $Sr_2Ru_2O_7$

inclusions and provides a direct, model-independent proxy for the impurity contribution to the magnetisation. Again, no systematic correlation is found. Taken together, the absence of correlation with both C and χ_{max} argues strongly against magnetic impurities as the primary origin of the BTRS-related signal below T_{c}.

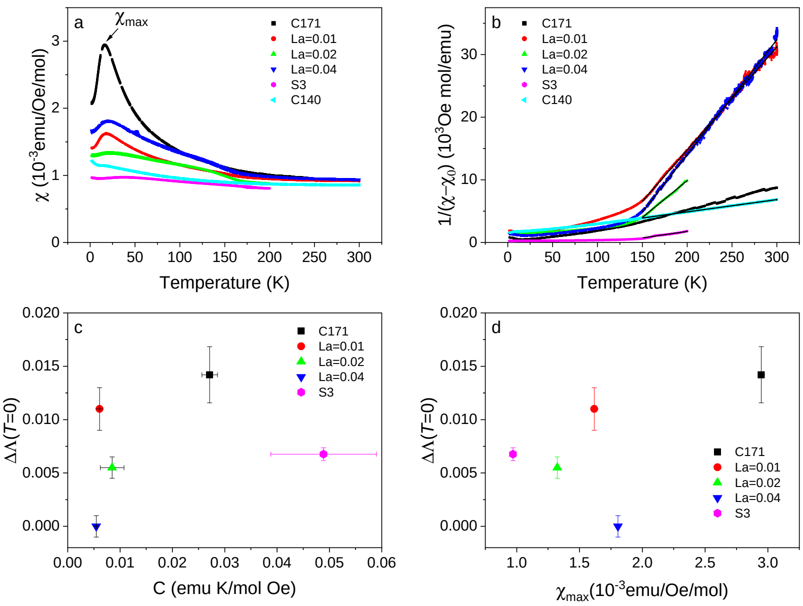

Fig. S6 Magnetic susceptibility analysis. (a) Magnetic susceptibility $\chi(T)$ for Sr_2RuO_4 samples: C171, C140, S3, and La-doped samples measured at $B = 1$ T ($H \parallel ab$). Both zero-field-cooled (ZFC) and field-cooled (FC) curves are shown, with no pronounced difference observed between the two. The solid lines represent fits to Eq. (2) for $T > 150$ K. (b) Inverse susceptibility after subtracting the linear nonmagnetic background, $1/(\chi - \chi_0)$. The linearity confirms Curie-Weiss behavior. (c) Enhanced muon-spin relaxation rate $\Delta\Lambda(T = 0)$ in the superconducting state versus the Curie constant C for various samples. (d) $\Delta\Lambda(T = 0)$ versus a maximum measured value of the magnetic susceptibility χ_{max} as illustrated in panel a. In both (c) and (d), the absence of a proportional relationship indicates that magnetic impurities are unlikely to be the source of the enhanced muon-spin relaxation rate below T_{c}.

7 Absence of Extended Structural Defects

To assess the possible role of extended structural defects such as dislocations in generating the spontaneous magnetic fields, we performed transmission electron microscopy (TEM) and scanning transmission electron microscopy (STEM) on representative Sr_2RuO_4 single crystals (samples S3 and C140). TEM investigations were performed in a Talos F200X FEG-(S) TEM (FEI) with 200 keV acceleration voltage on samples prepared by focused ion beam.

Focused-ion-beam (FIB) lamellae were first prepared from sample S3 and thinned by argon ion milling. Two lamellae with different initial crystallographic orientations relative to the TEM grid (Lamella A and Lamella B) were examined. Although linear contrast features were initially visible, a comparison of the two lamellae showed that these features are topographic artifacts related to surface facets and thickness gradients induced during sample preparation. As shown in Fig. S7(a), the linear features appear at the same angle (55°) relative to the STEM scan direction in both lamellae, demonstrating that they do not represent intrinsic internal defects.

To test explicitly for pre-existing dislocation networks, sample C140 was used in a multi-angle tilting STEM experiment. FIB lamellae from this sample were examined along three widely separated crystallographic zone axes (ZA_[010], ZA_[120], and ZA_[7-3-1]) using large-angle tilting in the TEM. This approach ensures that any existing dislocations, regardless of the direction of their Burgers vector, would satisfy the visibility criterion ($\mathbf{g} \cdot \mathbf{b} \neq 0$) in at least one orientation. Across all observed zone axes, however, neither STEM dark-field images [Fig. S7(b)] nor conventional bright-field micrographs revealed identifiable dislocations. Based on the total analyzed volume of approximately 3.7 μm^3, the upper bound for the dislocation density is estimated to be below 10^{11} m^{-2}.

The dislocation density found in these measurements indicates that extended defect networks are unlikely to account for the volume-sensitive time-reversal-symmetry-breaking signal observed in ZF-μSR.

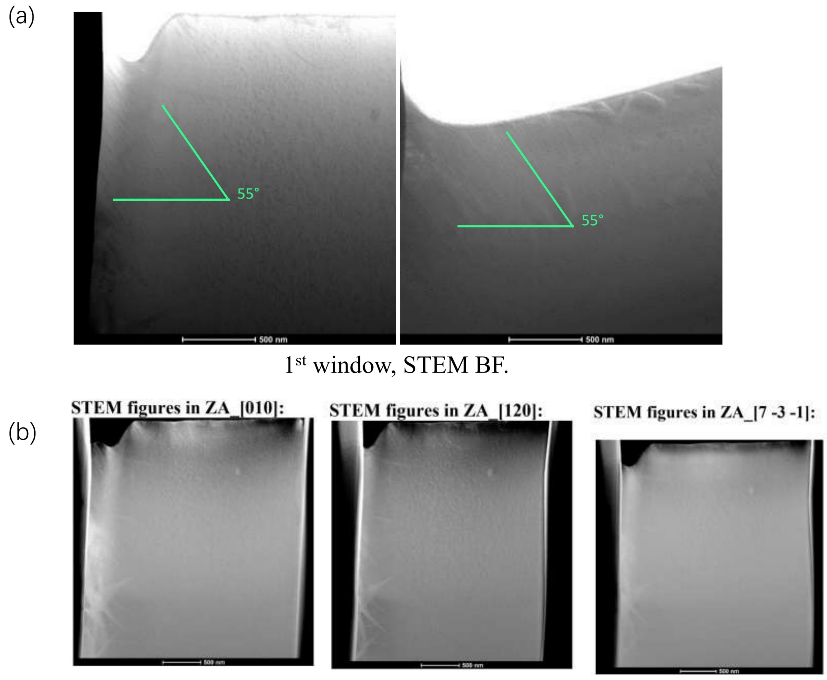

Fig. S7 Absence of extended defects and limits on dislocation density in pristine Sr_2RuO_4 single crystals. (a) STEM bright-field images of two differently oriented FIB lamellae (Lamella A and Lamella B) from sample S3. The linear contrast features appear at an identical angle (55°) in both lamellae, confirming that they are surface topography artifacts from argon ion milling rather than intrinsic internal structural defects. (b) Representative STEM dark-field micrographs of sample C140 recorded along three different zone axes (ZA_[010], ZA_[120], and ZA_[7-3-1]). The multi-angle tilting experiment indicates a pristine crystal lattice without observable dislocations, yielding an upper bound on the dislocation density of $< 10^{11}$ m^{-2}.